


RESEARCH ARTICLE | JANUARY 19 2023

Frequency response of cantilevered plates of small aspect ratio immersed in viscous fluids

Naijian Shen ; Debadi Chakraborty; John E. Sader  *J. Appl. Phys.* 133, 034501 (2023)<https://doi.org/10.1063/5.0120736>

CrossMark

Export
Citation

Articles You May Be Interested In

Use of the Spanish adaptation of the phonetic and phonologic Ling tests to evaluate progress in children with cochlear implants and hearing aids

J Acoust Soc Am (October 2002)

Word constraints on syllable identification

J Acoust Soc Am (May 1981)

Rhythmic processes in Spanish

J Acoust Soc Am (August 2005)

500 kHz or 8.5 GHz? And all the ranges in between.

Lock-in Amplifiers for your periodic signal measurements

[Find out more](#) Zurich
Instruments

Frequency response of cantilevered plates of small aspect ratio immersed in viscous fluids

Cite as: J. Appl. Phys. **133**, 034501 (2023); doi: [10.1063/5.0120736](https://doi.org/10.1063/5.0120736)

Submitted: 14 August 2022 · Accepted: 24 December 2022 ·

Published Online: 19 January 2023



Naijian Shen,^{1,2}  Debadi Chakraborty,² and John E. Sader^{3,a)} 

AFFILIATIONS

¹The Fluid Dynamics of Disease Transmission Laboratory, Massachusetts Institute of Technology, Cambridge, Massachusetts 02139, USA

²School of Mathematics and Statistics, The University of Melbourne, Victoria 3010, Australia

³Graduate Aerospace Laboratories, California Institute of Technology, Pasadena, California 91125, USA

^{a)}Author to whom correspondence should be addressed: jsader@caltech.edu

ABSTRACT

Comprehensive theoretical models for the dynamic response of slender cantilevered beams immersed in fluid have been widely reported, while the distinct behavior of wide cantilevered plates has received comparatively little attention. In this article, we develop an exact analytical theory for the resonant response of rectangular cantilevered plates of zero length-to-width aspect ratio that are immersed in unbounded viscous fluids. Unlike the opposite slender limit of large aspect ratio, the hydrodynamic load experienced by zero-aspect-ratio cantilevered plates is inherently non-local, which can strongly affect the individual mode shapes of the plate. In addition, finite-element-method simulations are reported for two- and three-dimensional cases of zero and finite aspect ratio, respectively. Accuracy of the present theory and that of Atkinson and Manrique de Lara [J. Sound Vib. **300**, 352 (2007)] for small viscosity and zero aspect ratio is assessed using the former simulations. The latter simulations are used to clarify the regime of validity of the present theory as a function of aspect ratio, along with that of existing theory for slender (large aspect ratio) beams. The results of this study are expected to be of practical importance to micro- and nano-electromechanical system design and their applications.

09 October 2023 17:49:51

Published under an exclusive license by AIP Publishing. <https://doi.org/10.1063/5.0120736>

I. INTRODUCTION

The dynamics of cantilevered devices are pertinent to a wide range of applications, including imaging and force spectroscopy with atomic force microscopy (AFM),^{1–5} energy harvesting,⁶ microfluidic sensing,^{7,8} and mass spectroscopy using micro- and nano-electromechanical systems (MEMS and NEMS, respectively).^{9–11} In many of these applications, a cantilevered structure is immersed in a fluid environment that strongly affects its dynamic response, relative to its operation in vacuum. For cantilevers of macroscopic scale, fluid viscosity typically exerts a negligible effect with hydrodynamic loading enhancing the effective inertial mass of the cantilever—thereby lowering its resonant frequencies.^{12–15} In contrast, it has been shown that the dynamics of microscale cantilevers are significantly affected by the viscosity of the surrounding fluid, enhancing both the inertial load and energy dissipation.^{3,5,16–18} This dissipation is often quantified by the quality factor (*Q*-factor) of each resonant mode, which is proportional to the ratio of the

maximum elastic energy stored in the structure to dissipation in one cycle of oscillation.

The hydrodynamic load acting on a slender cantilevered beam immersed in a fluid is often assumed to depend locally on the cantilever displacement, an approximation that holds provided the cantilever length greatly exceeds its width.^{5,12,18} This approach provides an accurate framework that has enabled comprehensive studies of the dynamics of cantilevered beams in fluid. Chu¹² presented an early and widely used formula for the resonant frequencies of a slender cantilever beam immersed in an inviscid fluid, which was validated experimentally.¹³ Sader¹⁸ showed that this inviscid fluid approximation deteriorates as the cantilever size is reduced—relevant to modern applications in AFM, MEMS, and NEMS—with fluid viscosity exerting an increasing effect. He developed a theory that incorporates the role of viscosity, which was found to be accurate for the first few flexural resonant modes of practical AFM microcantilevers.^{19–21} Expanding on the approach of Elmer and Drier,¹⁷ van Eysden

and Sader¹⁵ developed analytical formulas that accounted for the three-dimensional nature of inviscid flows, generated by slender cantilever beams vibrating in their higher-order flexural and torsional modes. These authors later extended their theory to rigorously account for the effects of fluid viscosity and compressibility.^{5,22–24}

The above-mentioned locality of the hydrodynamic load for slender beams deteriorates as the length-to-width aspect ratio of the cantilevered plate decreases, with the dynamic response of wide cantilevered plates differing markedly from their slender counterparts. Moreover, non-conventional transverse modes can be excited by low aspect ratio plate-type resonators in liquid,²⁵ with a recent numerical study reporting a distinct displacement spectrum for these modes.²⁶ Despite the behavioral shift as the aspect ratio is reduced and the existence of moderate-to-low aspect ratio cantilevers in practice, analytical results for wide cantilevered plates are scant. Notably Lindholm *et al.*,¹³ drawing on the work of Pabst²⁷ from 1930, proposed empirical correction factors to the (infinite aspect ratio) formula of Chu,¹² to accommodate cantilevered plates of finite and smaller aspect ratio. The resulting theory produced a reasonable agreement with measurements at the time.

In a more recent advance, Atkinson and Manrique de Lara²⁸ theoretically studied the limit of zero aspect ratio, i.e., a two-dimensional cantilevered plate that is infinitely wide relative to its length and immersed in an inviscid fluid, where it was reported that the corresponding hydrodynamic pressure depends non-locally on the entire deflected mode shape. Shen *et al.*²⁹ expanded on this previous study and explored the effect of varying the clamping condition—which exerts a strong effect on the dynamic response due to non-locality of the flow—and provided simple formulas for flexural resonant frequencies. These zero-aspect-ratio formulas were connected with corresponding literature results for large (infinite) aspect ratio, producing general formulas for arbitrary aspect ratio that display excellent agreement with independent direct numerical simulations. This highlighted deficiencies in the empirical aspect-ratio correction formulas of Lindholm *et al.*¹³ (based on Pabst²⁷), which are erroneously independent of the clamp condition. The theoretical models mentioned in this and the preceding paragraphs consider the hydrodynamic flow to be inviscid and are, thus, generally restricted to cantilevered plates of macroscopic size.

In this article, we expand on the study of Shen *et al.*²⁹ to rigorously include the effects of fluid viscosity, which is directly relevant to applications involving small cantilevered plates used in AFM, MEMS, and NEMS. The theoretical development initially focuses on cantilevered plates of zero aspect ratio. Formulas are given for both the resonant frequencies and Q -factors of flexural modes. We also report high-accuracy finite-element-method simulations of the fluid-structure interaction, for zero and finite aspect ratio, to benchmark the developed theory. These results highlight the validity of the developed theory for zero aspect ratio and arbitrary mode number. In contrast, the small viscosity theory of Atkinson and Manrique de Lara²⁸ is found to be relatively inaccurate for the numerical range studied; a potential reason of which is discussed. A comparison is also made to the existing theory for large aspect

ratio.^{18,30} These comparisons to finite-element-method simulations show that the zero and large aspect ratio theories can be used together to characterize the resonant response for cantilevered plates of arbitrary aspect ratio.

II. THEORY FOR ZERO-ASPECT-RATIO CANTILEVERED PLATES

We begin by explicating the principal assumptions of the present analysis. A cantilevered plate of rectangular plan view geometry with length L , width b , and thickness h is studied. The plate thickness is infinitesimally small relative to both its width and length, i.e., $h/b, h/L \rightarrow 0$. In this section, we consider the zero-aspect-ratio limit only, i.e., $b/L \rightarrow 0$; this restriction is relaxed in later sections. While Shen *et al.*²⁹ studied a variety of clamp conditions, here we focus only on the so-called “line clamp.” Namely, one edge of the plate of width b , is clamped into a thin rigid cylinder (much narrower than the cantilever length) that is restrained from rotating, while the other plate edge is free to oscillate at angular frequency, ω . A schematic illustration of this configuration is given in Fig. 1. A Cartesian coordinate system is used such that the undeflected cantilevered plate lies in the x - y plane, with the clamped end at $x = -L/2$ and the free end at $x = L/2$; its origin is at the center-of-mass of the plate.

As for slender cantilevered beams considered by Sader,¹⁸ only the flexural modes of oscillation are studied here. Specifically, the cantilever displacement is independent of the y -coordinate. The vibration amplitude of the cantilevered plate is assumed to be infinitesimally small relative to all plate dimensions. As such, plate deformation obeys the small deflection theory of thin plates,³¹ and the flow generated by such a mechanical structure is governed by the linearized Navier–Stokes equations.³² The viscous fluid surrounding the cantilevered plate is unbounded and considered to be incompressible, i.e., all wave effects in the fluid are ignored, which is a valid approximation provided the mode number is not too large.²⁴

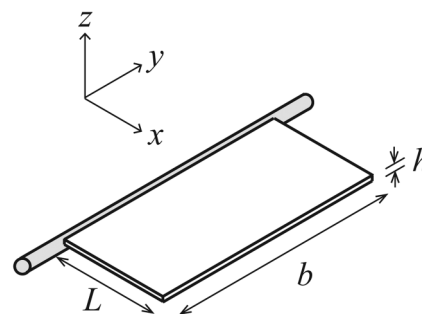


FIG. 1. Schematic illustration of a rectangular cantilevered plate with a “line clamp,” i.e., a rigid rod whose thickness is far smaller than the plate length. The Cartesian coordinate system used in the analysis is as indicated, with its origin at the center-of-mass of the plate.

09 October 2023 17:49:51

A. Governing equations

For a thin elastic plate of zero aspect ratio, i.e., $L/b \rightarrow 0$, its dynamic deflection function, $w(x, t)$, in the z -direction, is governed by³¹

$$D \frac{\partial^4 w}{\partial x^4} + \rho_c h \frac{\partial^2 w}{\partial t^2} = P, \quad (1)$$

where $D \equiv Eh^3/(12[1 - \nu^2])$ is the flexural rigidity of the plate, E is its Young's modulus, ν is its Poisson's ratio, ρ_c is its mass density, t is time, and P is the applied force per unit area in the z -direction; see Fig. 1 for the Cartesian coordinate system. The associated boundary conditions are

$$w\left(-\frac{L}{2}, t\right) = \frac{\partial w}{\partial x}\bigg|_{x=-\frac{L}{2}} = \frac{\partial^2 w}{\partial x^2}\bigg|_{x=-\frac{L}{2}} = \frac{\partial^3 w}{\partial x^3}\bigg|_{x=-\frac{L}{2}} = 0. \quad (2)$$

Motion of the plate drives a two-dimensional flow, in the (x, z) -plane, in the viscous fluid that surrounds it. This flow is governed by the linearized incompressible Navier–Stokes equations,³²

$$\nabla \cdot \mathbf{u} = 0, \quad \rho \frac{\partial \mathbf{u}}{\partial t} = -\nabla p + \mu \nabla^2 \mathbf{u}, \quad (3)$$

where $\mathbf{u}(x, z, t)$ is the velocity field, $p(x, z, t)$ is the hydrodynamic pressure field, ρ is the fluid density, and μ is the shear viscosity of the fluid. Its associated boundary conditions are no-slip at the plate surface with vanishing flow far from the plate. Moreover, the force per unit area, P , experienced by the plate is related to the hydrodynamic pressure, p , by

$$P(x, t) = p(x, 0^-, t) - p(x, 0^+, t) = -2p(x, 0^+, t), \quad (4)$$

by symmetry of the flow. This closes the problem with the above equations defining a coupled fluid–structure interaction problem for the cantilevered plate immersed in an unbounded viscous fluid.

Due to linearity of the governing equations, we utilize the time ansatz,

$$X(t) = \bar{X}(\omega)e^{-i\omega t}, \quad \omega \in \mathbb{C}, \quad (5)$$

for all dependent variables, where $X(t)$ is a generic function of time and i is the imaginary unit. Complex-valued frequencies, ω , are used to account for conservative (real) and dissipative (imaginary) effects. The superfluous bar symbol in Eq. (5) will be omitted, henceforth, for simplicity, with all time-dependent variables referring to their frequency-domain forms.

Next, we non-dimensionalize the governing equations. The cantilever displacement is scaled by the oscillation amplitude at its free end, $a \equiv w(L/2)$; the spatial coordinates are scaled by the cantilever length, L ; time is scaled by ω^{-1} ; the fluid velocity is scaled by $a\omega$; and the hydrodynamic pressure is scaled by the inertial

scale, $a\rho\omega^2 L$. Equations (1) and (2) then become

$$\frac{d^4 w}{dx^4} - \Omega^2 w = \Lambda \Omega^2 P, \quad (6a)$$

$$w\left(-\frac{1}{2}\right) = w'\left(-\frac{1}{2}\right) = w''\left(\frac{1}{2}\right) = w'''\left(\frac{1}{2}\right) = 0 \quad (6b)$$

where

$$\Omega \equiv \omega L^2 \sqrt{\frac{\rho_c h}{D}}, \quad \Lambda \equiv \frac{\rho L}{\rho_c h}, \quad (7)$$

are (i) the dimensionless oscillation frequency [scaled by a natural plate frequency; see Eq. (13)] and (ii) the added mass parameter that specifies the strength of the hydrodynamic load (scaled by the inertial load of the plate), respectively. Similarly, Eq. (3) becomes

$$\nabla \cdot \mathbf{u} = 0, \quad -i\mathbf{u} = -\nabla p + \frac{1}{\beta} \nabla^2 \mathbf{u}, \quad (8)$$

with the oscillatory Reynolds number,

$$\beta \equiv \frac{\rho\omega L^2}{\mu}. \quad (9)$$

Henceforth, all variables refer to their dimensionless frequency-domain forms, unless otherwise specified.

1. Basis modes for the cantilevered plate

The eigenvalue problem corresponding to Eq. (6a) is

$$\frac{d^4 \Phi_n}{dx^4} - C_n^4 \Phi_n = 0, \quad (10)$$

with identical boundary conditions to Eq. (6b), where Φ_n is the n th eigenmode,¹⁸

$$\begin{aligned} \Phi_n(x) = & \cos\left(C_n\left[x + \frac{1}{2}\right]\right) - \cosh\left(C_n\left[x + \frac{1}{2}\right]\right) + \frac{\cos C_n + \cosh C_n}{\sin C_n + \sinh C_n} \\ & \times \left\{ \sinh\left(C_n\left[x + \frac{1}{2}\right]\right) - \sin\left(C_n\left[x + \frac{1}{2}\right]\right) \right\}, \end{aligned} \quad (11)$$

whose eigenvalue, C_n , is given by the n th positive root of

$$\cos C_n \cosh C_n = -1. \quad (12)$$

These eigenmodes form a complete and orthonormal basis set, i.e., $\int_{-\frac{1}{2}}^{\frac{1}{2}} \Phi_j \Phi_k dx = \delta_{jk}$, where δ_{jk} is the Kronecker delta function. They are used in Sec. II B 1 to generally represent the deflection function, w , in the presence of fluid loading.

The basis function, Φ_n , corresponds to the n th resonant mode of the cantilevered plate in the absence of fluid, i.e., in vacuum, whose (dimensional) resonant frequency is

$$\omega_{\text{vac},n} = \frac{C_n^2}{L^2} \sqrt{\frac{D}{\rho_c h}}. \quad (13)$$

B. Two-dimensional flow field of the surrounding fluid

Next, we calculate the non-local hydrodynamic load experienced by the zero-aspect-ratio cantilevered plate immersed in a viscous fluid; due to the two-dimensional nature of the flow in the (x, z) -plane, this load is independent of the y -coordinate.

1. Basis flow expansion

To construct the flow field produced by the moving cantilevered plate, we employ the approach of van Eysden and Sader.²² This utilizes the three-dimensional basis flow generated above an infinite solid surface executing normal harmonic oscillations in both x and y -directions at a frequency of ω , as per Eq. (5). The (dimensionless) displacement function of this surface is

$$Z(x, y) = e^{i\lambda x} e^{i\kappa y}, \quad (14)$$

where λ and κ are wave numbers in x - and y -directions, respectively. The corresponding solution to Eq. (8) for this basis flow is reported in Ref. 22, where the $\kappa \rightarrow 0$ limit is taken to obtain the required two-dimensional base flow in the (x, z) -plane. The velocity and pressure fields produced by the cantilevered plate can then be determined from this basis flow using the principle of linear superposition. First, the z -component of the velocity field, u_z , and the pressure field, p , are constructed, giving

$$u_z(x, z) = -i \lim_{\kappa \rightarrow 0} \int_0^\infty [\chi(\lambda|\kappa, \beta) \cos(\lambda x) + \psi(\lambda|\kappa, \beta) \sin(\lambda x)] \times \left(\sqrt{\lambda^2 + \kappa^2} e^{-z\sqrt{\lambda^2 + \kappa^2}} - \frac{\lambda^2 + \kappa^2}{\sqrt{\lambda^2 + \kappa^2} - i\beta} e^{-z\sqrt{\lambda^2 + \kappa^2 - i\beta}} \right) d\lambda, \quad (15a)$$

$$p(x, z) = - \lim_{\kappa \rightarrow 0} \int_0^\infty [\chi(\lambda|\kappa, \beta) \cos(\lambda x) + \psi(\lambda|\kappa, \beta) \sin(\lambda x)] e^{-z\sqrt{\lambda^2 + \kappa^2}} d\lambda, \quad (15b)$$

where the kernel functions, $\chi(\lambda|\kappa, \beta)$ and $\psi(\lambda|\kappa, \beta)$, are to be determined from the boundary conditions; y -independence of this two-dimensional flow is imposed by the limit, $\kappa \rightarrow 0$.

Boundary conditions are specified at the plate surface, $z = 0$,²² by

$$u_z(x, 0) = -i\omega, \quad |x| \leq \frac{1}{2}, \quad (16a)$$

$$p(x, 0) = 0, \quad |x| > \frac{1}{2}, \quad (16b)$$

with the flow vanishing far from the plate. As foreshadowed in Sec. II A 1, the deflection function of the cantilevered plate, w , under hydrodynamic loading can be constructed using the general expansion,

$$w(x) = \sum_{k=1}^N a_k \Phi_k(x), \quad (17)$$

where the coefficients, a_k , are to be determined from the fluid-structure interaction, and the number of terms, N , is to be increased systematically to achieve convergence.

2. Evaluation of kernel functions

Substituting Eqs. (15) and (17) into Eq. (16) gives

$$\lim_{\kappa \rightarrow 0} \int_0^\infty \chi_k(\lambda|\kappa, \beta) \cos(\lambda x) \sqrt{\lambda^2 + \kappa^2} \left(1 - \frac{\sqrt{\lambda^2 + \kappa^2}}{\sqrt{\lambda^2 + \kappa^2} - i\beta} \right) d\lambda = \Phi_k \text{even}(x) \quad (18a)$$

$$\lim_{\kappa \rightarrow 0} \int_0^\infty \psi_k(\lambda|\kappa, \beta) \sin(\lambda x) \sqrt{\lambda^2 + \kappa^2} \left(1 - \frac{\sqrt{\lambda^2 + \kappa^2}}{\sqrt{\lambda^2 + \kappa^2} - i\beta} \right) d\lambda = \Phi_k \text{odd}(x) \quad (18b)$$

for $|x| \leq 1/2$, and

$$\int_0^\infty \chi_k(\lambda|\kappa, \beta) \cos(\lambda x) d\lambda = \int_0^\infty \psi_k(\lambda|\kappa, \beta) \sin(\lambda x) d\lambda = 0, \quad |x| > \frac{1}{2}, \quad (19)$$

where we have introduced the even and odd components of the eigenmodes,

$$\begin{aligned} \Phi_k \text{even}(x) &\equiv \frac{1}{2} [\Phi_k(x) + \Phi_k(-x)], \\ \Phi_k \text{odd}(x) &\equiv \frac{1}{2} [\Phi_k(x) - \Phi_k(-x)]. \end{aligned} \quad (20)$$

The two sets of decomposed kernel functions, $\chi_k(\lambda|\kappa, \beta)$ and $\psi_k(\lambda|\kappa, \beta)$, are defined in accordance to Eq. (17),

$$\begin{aligned}\chi(\lambda|\kappa, \beta) &= \sum_{k=1}^N a_k \chi_k(\lambda|\kappa, \beta), \\ \psi(\lambda|\kappa, \beta) &= \sum_{k=1}^N a_k \psi_k(\lambda|\kappa, \beta).\end{aligned}\quad (21)$$

To evaluate χ_k and ψ_k , we use the ansatz,^{17,22}

$$\begin{aligned}\chi_k(\lambda|\kappa, \beta) &= \sum_{m=1}^M b_{m,k} J_{2m-2}\left(\frac{\lambda}{2}\right), \\ \psi_k(\lambda|\kappa, \beta) &= \sum_{m=1}^M c_{m,k} J_{2m-1}\left(\frac{\lambda}{2}\right),\end{aligned}\quad (22)$$

where M is the series truncation number and J_ν is the Bessel function of the first kind of order ν , whereas $b_{m,k}$ and $c_{m,k}$ are coefficients to be determined from Eq. (18) that implicitly depend on the oscillatory Reynolds number, β . Equation (22) ensures satisfaction of Eq. (19),³³ and the pressure distribution exhibits the required square root singularities at the plate edges, $|x| = 1/2$. This behavior is readily observed by substituting Eq. (22) into Eq. (15b), yielding the following expression for the pressure on the upper surface of the plate,

$$p(x, 0^+) = - \sum_{k=1}^N a_k H_k(x), \quad (23)$$

with

$$H_k(x) = \frac{2}{\sqrt{1-4x^2}} \sum_{m=1}^M \left[b_{m,k} T_{2m-2}(\sqrt{1-4x^2}) + 2c_{m,k} x U_{2m-2}(\sqrt{1-4x^2}) \right], \quad (24)$$

where T_m and U_m are Chebyshev polynomials of the first and second kinds of order m , respectively; the dependence on the oscillatory Reynolds number, β , is implicit through the coefficients, $b_{m,k}$ and $c_{m,k}$.

Note that this singular behavior in the pressure at the plate edges, $|x| = 1/2$, does not occur for the inviscid flow (where the pressure is zero at $|x| = 1/2$). Thus, an alternate ansatz to Eq. (22) is needed for the inviscid solution. An exact solution for the inviscid flow that uses the above approach with such an alternate ansatz is given in Appendix A; it provides a different, but equivalent, solution to that reported in Ref. 29.

Substituting Eq. (22) into Eq. (18) and then expanding the resulting equations in power series in x generates the following systems of linear equations for the coefficients $b_{m,k}$ and $c_{m,k}$,

$$\sum_{m=1}^M B_{q,m} b_{m,k} = (-1)^{q-1} \frac{d^{2q-2}}{dx^{2q-2}} \Phi_k \text{even}(x) \Big|_{x=0}, \quad (25a)$$

$$\sum_{m=1}^M C_{q,m} c_{m,k} = (-1)^{q-1} \frac{d^{2q-1}}{dx^{2q-1}} \Phi_k \text{odd}(x) \Big|_{x=0}, \quad (25b)$$

where $q = 1, 2, \dots, M$, and $k = 1, 2, \dots, N$ [see Eq. (21)]; the coefficients, $B_{q,m}$ and $C_{q,m}$, are improper integrals that can be specified in terms of Meijer G -functions,

$$\begin{aligned}B_{q,m} &= - \frac{4^{2q-1}}{\sqrt{\pi}} \lim_{\kappa \rightarrow 0} G_{1,3}^{2,1} \left(\frac{\kappa^2}{16} \middle| 0, q+m-1, q-m+1 \right) \\ &\quad - \frac{2^{4q-1}}{\sqrt{\pi}} G_{1,3}^{2,1} \left(\frac{-i\beta}{16} \middle| 0, q+m-1, q-m+1 \right),\end{aligned}\quad (26a)$$

$$\begin{aligned}C_{q,m} &= - \frac{4^{2q}}{\sqrt{\pi}} \lim_{\kappa \rightarrow 0} G_{1,3}^{2,1} \left(\frac{\kappa^2}{16} \middle| 0, q+m, q-m+1 \right) \\ &\quad - \frac{2^{4q+1}}{\sqrt{\pi}} G_{1,3}^{2,1} \left(\frac{-i\beta}{16} \middle| 0, q+m, q-m+1 \right).\end{aligned}\quad (26b)$$

A derivation of these results is given in Appendix B. The limits in Eq. (26) can be evaluated to give

$$B_{q,m} = 2^{4q-1} \left[\frac{\Gamma(m+q-1)}{\Gamma(m-q)} - \frac{1}{\sqrt{\pi}} G_{1,3}^{2,1} \left(\frac{-i\beta}{16} \middle| 0, q+m-1, q-m+1 \right) \right], \quad (27a)$$

$$C_{q,m} = 2^{4q+1} \left[\frac{\Gamma(m+q)}{\Gamma(m-q)} - \frac{1}{\sqrt{\pi}} G_{1,3}^{2,1} \left(\frac{-i\beta}{16} \middle| 0, q+m, q-m+1 \right) \right], \quad (27b)$$

where Γ here refers to the Gamma function (not the hydrodynamic function).

Solving the independent linear systems in Eq. (25) for the coefficients, $b_{m,k}$ and $c_{m,k}$, substituting those solutions into Eq. (22) and subsequently into Eqs. (15) and (21), gives the required results for the velocity and pressure fields.

C. Frequency response of the cantilevered plate

It follows from Eqs. (4), (6a), (7), (13), and (23) that the resonant response of the n th mode of the cantilevered plate is characterized by two dimensionless parameters,

$$\bar{\beta}_n = \frac{\rho \omega_{\text{vac},n} L^2}{\mu}, \quad \Lambda = \frac{\rho L}{\rho_c h}, \quad (28)$$

where $\bar{\beta}_n$ is the normalized Reynolds number of mode n , specifying the relative magnitude of inertial to viscous forces in the fluid; and Λ is the ratio of fluid-to-solid inertia defined in Eq. (7), which dictates the relative strength of fluid loading.

Substituting Eqs. (4) and (17) into Eq. (6a), while using Eq. (10) and the orthonormality of Φ_j , gives

$$\sum_{k=1}^N a_k \left[\left(\frac{C_k^4}{C_n^4} - \Omega_n^2 \right) \delta_{jk} - 2\Omega_n^2 \Lambda \int_{-\frac{1}{2}}^{\frac{1}{2}} \Phi_j H_k dx \right] = 0, \quad (29)$$

for $n, j = 1, 2, \dots, N$, and

$$\Omega_n \equiv \frac{\omega_n}{\omega_{\text{vac},n}}, \quad (30)$$

where ω_n is the (dimensional) complex resonant frequency in fluid of mode n . Note that the oscillatory Reynolds number, β , is recovered from the expression, $\beta \equiv \Omega_n \bar{\beta}_n$.

The eigenvalue problem in Eq. (29) is to be solved for a specific normalized Reynolds number, $\bar{\beta}_n$, and added mass parameter, Λ . The resulting coefficients, a_k , specify the deflection function of the n th mode of the cantilevered plate in fluid and its hydrodynamic pressure distribution via Eqs. (17) and (23), respectively.

The required (real-valued) angular resonant frequency, $\omega_{R,n}$, and corresponding quality factor, Q_n , of mode n are then given by³⁴

$$\omega_{R,n} = \sqrt{\omega_{r,n}^2 + \omega_{i,n}^2}, \quad Q_n = -\frac{\sqrt{\omega_{r,n}^2 + \omega_{i,n}^2}}{2\omega_{i,n}}, \quad (31)$$

where $\omega_{r,n}$ and $\omega_{i,n}$ are the real and imaginary parts of ω_n , respectively. These formulas specify the frequency response of the cantilevered plate. They are derived under the assumption of small dissipation, i.e., $Q_n \gg 1$, where the hydrodynamic load of each mode is insensitive to frequency.

D. Hydrodynamic function

The effect of fluid loading on the frequency response of cantilevered beams and plates is often characterized by the (complex-

valued) hydrodynamic function, $\Gamma = \Gamma_r + i\Gamma_i$,^{5,18} such that

$$\frac{\omega_{R,n}}{\omega_{\text{vac},n}} = \left[1 + \frac{\pi \rho b}{4 \rho_c h} \Gamma_r(\omega_{R,n}, n) \right]^{-\frac{1}{2}}, \quad Q_n = \frac{\frac{4 \rho_c h}{\pi \rho b} + \Gamma_i(\omega_{R,n}, n)}{\Gamma_r(\omega_{R,n}, n)}. \quad (32)$$

In the large aspect ratio limit, $L/b \gg 1$, explicit expressions for $\Gamma = \Gamma_{\text{large}}$ are reported in Refs. 5 and 18; the effect of finite plate thickness is discussed in Ref. 30. For the opposite limit of small aspect ratio, $L/b \ll 1$, it follows from Eq. (29) that

$$\Gamma = \Gamma^{\text{small}} \equiv \frac{4L}{\pi b} \alpha^{\text{small}}, \quad \frac{L}{b} \ll 1, \quad (33)$$

where α^{small} is an order one function, henceforth termed the “rescaled hydrodynamic function,” that depends on the added mass parameter, Λ . The superscripts “small” and “large” are used to delineate different regimes in aspect ratio, L/b .

Numerically, the real and imaginary parts of α^{small} for each mode number, n , are computed using Eqs. (30)–(33), giving

$$\alpha_r^{\text{small}} = \frac{|\Omega_n|^{-2} - 1}{\Lambda}, \quad \alpha_i^{\text{small}} = -\frac{2 \text{Im}\{\Omega_n\}}{\Lambda |\Omega_n|^3}, \quad (34)$$

where Ω_n is obtained by solving the eigenvalue problem, Eq. (29).

Additionally, in the large mode number limit, $n \gg 1$,^{5,17,22}

$$\Gamma \equiv \frac{4L}{\pi b} \alpha = \frac{8L}{\pi C_n b} \frac{\sqrt{C_n^2 - i\beta}}{\sqrt{C_n^2 - i\beta} - C_n}, \quad n \gg \frac{L}{b}, \quad (35)$$

regardless of the aspect ratio, L/b , where α is defined in an identical manner to α^{small} in Eq. (33). A comparison of Eq. (35) to the solution for arbitrary mode number in Eq. (34), is given in Sec. SM 1 of the [supplementary material](#).

In the next section, we present numerical results arising from implementation of the zero-aspect-ratio theory developed above. This theory is validated using high accuracy finite-element-method simulations of the fluid-structure problem, and a detailed comparison with the small viscosity theory of Atkinson and Manrique de Lara²⁸ is reported.

III. NUMERICAL RESULTS FOR ZERO ASPECT RATIO

The theory in Sec. II C is implemented in mathematica. The number of terms, M , in Eq. (22) and the number of eigenmodes, N , in Eq. (17)—that are required to achieve convergence greater than 99.9% in Ω_n —increase systematically with Reynolds number, β , and mode number, n , respectively. We find that $N = 10$ and $M = 20$, together with a tolerance of 10^{-7} for computing $|\Omega_n|$ from Eq. (29), gives the required accuracy for $n \leq 8$ and $\beta < 3000$. Implementation at larger values of β is limited by computational constraints.

A. Rescaled hydrodynamic function

The effects of fluid loading on a cantilevered plate of zero aspect ratio are described by the rescaled hydrodynamic function,

TABLE I. Rescaled hydrodynamic function, α^{small} , for the fundamental mode, $n = 1$, as a function of normalized Reynolds number $\bar{\beta}_1$, and added mass parameter, Λ . (a) Real component and (b) imaginary component.

		$\log_{10} \Lambda$										
$\log_{10} \bar{\beta}_1$		−3	−2.5	−2	−1.5	−1	−0.5	0	0.5	1	1.5	2
(a)	3	0.722 949	0.723 016	0.723 256	0.723 946	0.726 085	0.732 440	0.749 075	0.784 680	0.846 398	0.941 224	1.082 65
	2.5	0.828 391	0.828 535	0.828 988	0.830 410	0.834 803	0.847 764	0.881 908	0.955 773	1.086 87	1.298 39	1.641 44
	2	1.006 37	1.006 70	1.007 73	1.010 98	1.021 04	1.050 90	1.130 62	1.307 39	1.637 54	2.231 41	
	1.5	1.309 13	1.309 98	1.312 66	1.321 10	1.347 41	1.427 20	1.650 66	2.188 97			
	1	1.829 09	1.831 60	1.839 54	1.864 77	1.945 58	2.210 27	3.094 74				
	0.5	2.741 61	2.750 15	2.777 46	2.866 72	3.180 88	4.569 03					
	0	4.408 51	4.441 92	4.551 97	4.950 40	7.023 55						
	−0.5	7.644 06	7.792 70	8.340 20	11.4357							
	−1	14.4300	15.2192	20.0151								
	−1.5	29.9801	37.5995									
	−2	74.8036										
(b)	3	0.144 042	0.144 122	0.144 348	0.144 970	0.147 005	0.153 003	0.169 122	0.205 328	0.272 284	0.383 021	0.562 562
	2.5	0.258 542	0.258 695	0.259 179	0.260 699	0.265 412	0.279 462	0.317 500	0.404 308	0.570 720	0.865 278	1.394 05
	2	0.487 117	0.487 524	0.488 808	0.492 847	0.505 406	0.543 174	0.647 446	0.894 246	1.400 18	2.407 64	
	1.5	0.982 045	0.983 291	0.987 229	0.999 649	1.038 60	1.158 52	1.507 38	2.408 54			
	1	2.155 91	2.160 34	2.174 38	2.218 99	2.362 27	2.834 45	4.436 64				
	0.5	5.187 00	5.205 15	5.263 06	5.451 23	6.101 11	8.828 67					
	0	13.5424	13.6272	13.9032	14.8650	19.3368						
	−0.5	37.6400	38.0912	39.6571	47.0937							
	−1	109.343	112.153	125.276								
	−1.5	328.623	353.502									
	−2	1034.19										

α^{small} ; see Eq. (33). Accurate numerical values for the fundamental mode, i.e., $n = 1$, over a wide range of the normalized Reynolds number, $\bar{\beta}_n$, and added mass parameter, Λ , are reported in Table I. These results are compared to the small- Λ asymptotic formula for α^{small} in Appendix C. Numerical results for the next two higher-order modes, i.e., $n = 2, 3$, are provided in Sec. SM 2 of the supplementary material. Numerical solutions are populated only for parameters that produce a large quality factor, i.e., $Q_n > 1$, to ensure validity of the theory in Sec. II C.

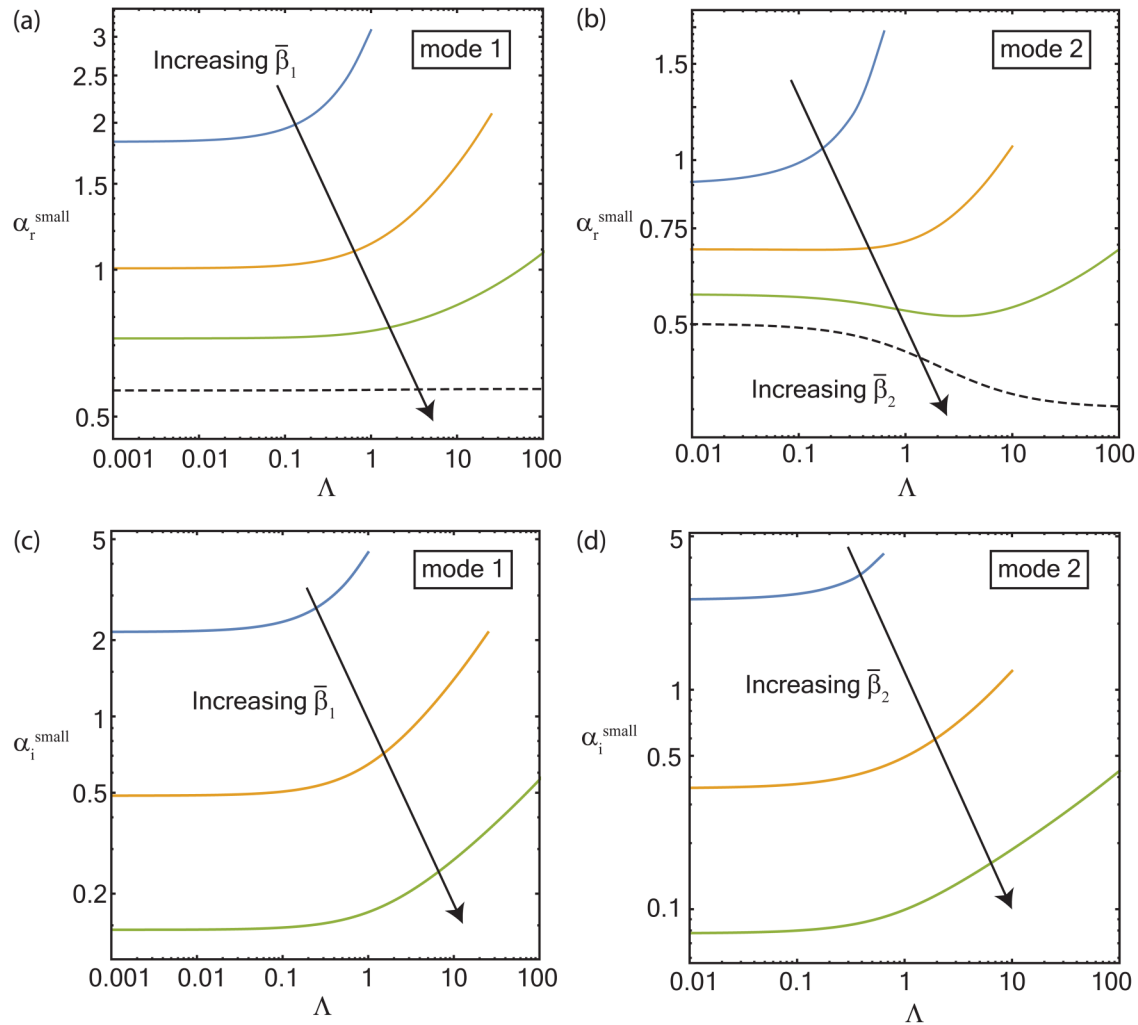
To explore these results, Fig. 2 gives the real and imaginary components of α^{small} as a function of Λ and $\bar{\beta}_n$ for the first two modes, $n = 1, 2$. The effect of fluid viscosity, characterized by the normalized Reynolds number, $\bar{\beta}_n$, is similar to that reported for large aspect ratio beams.^{5,18,22} Namely, increasing $\bar{\beta}_n$ reduces the viscous penetration depth, $\delta \sim 1/\sqrt{\beta}$ —the length scale for vorticity diffusion—which produces a monotonic decrease in both real and imaginary components of α^{small} , i.e., both inertial and viscous effects are diminished. However, the effect of varying the strength of fluid loading, Λ , is markedly different for zero and large aspect ratio plates, which we discuss next.

While the hydrodynamic function, Γ_{large} , in the large aspect ratio limit is not affected by the fluid loading strength at fixed oscillation frequency, i.e., constant β , the same is not true of the rescaled hydrodynamic function, α^{small} , for zero aspect ratio. The underlying mechanism for this difference in behavior is that (i) the hydrodynamic

load for large aspect ratio depends locally on the spatial position, x , while (ii) for zero aspect ratio, this load exhibits a non-local dependence on this position. This non-local dependence can result in modification of the resonant mode shapes of the cantilevered plate as the strength of fluid loading varies, altering the hydrodynamic function; this effect on the mode shapes is discussed in Sec. III B. For large aspect ratios, locality of the hydrodynamic load produces resonant mode shapes that are independent of fluid loading.^{5,18}

In addition to this mode shape change, the hydrodynamic load in a viscous fluid depends on β due to frequency dependence of the viscous penetration depth. Increasing the strength of fluid loading, Λ , enhances the inertial load experienced by the cantilevered plate, which lowers its resonant frequency—increasing the viscous penetration depth and thus the dimensionless hydrodynamic pressure. This is illustrated in Fig. 3, which shows that the dimensionless pressure distribution, $P(x)$, is enhanced by increasing the strength of fluid loading, Λ . Figure 3 also shows that the pressure distribution approaches the inviscid limit as $\bar{\beta}_n$ increases, except near the clamped and free ends of the plate, i.e., $x = -1/2$ and $1/2$, respectively, where square root singularities exist; see Eq. (23).

Figure 2, thus, demonstrates that the effect of mode shape change is most prevalent in the rescaled hydrodynamic function at small Λ and high $\bar{\beta}_n$. For example, see the viscous result for $\bar{\beta}_2 = 1000$ in Fig. 2(b) that follows the decreasing trend of the inviscid result with increasing Λ (affected by mode shape change only).²⁹



09 October 2023 17:49:51

FIG. 2. Real and imaginary parts of the rescaled hydrodynamic functions, α^{small} , for the first two resonant modes as a function of the added mass parameter, Λ . (a) and (c) are the real, α_r^{small} , and imaginary, α_i^{small} , parts respectively, for $n=1$; (b) and (d) for $n=2$. Results are given for normalized Reynolds number, $\bar{\beta}_n = 10, 100$, and 1000 , for both modes. In (a) and (b), α_r^{small} is also compared to the inviscid results (dashed curves), corresponding to $\bar{\beta}_n \rightarrow \infty$.

The effect of viscosity on the rescaled hydrodynamic function dominates the opposite limit of large Λ and small $\bar{\beta}_n$, inducing an increase in the rescaled hydrodynamic function (for reasons discussed in the previous paragraph). Note that the $n=1$ mode shape is insensitive to fluid loading relative to the higher order modes; see Fig. 4.

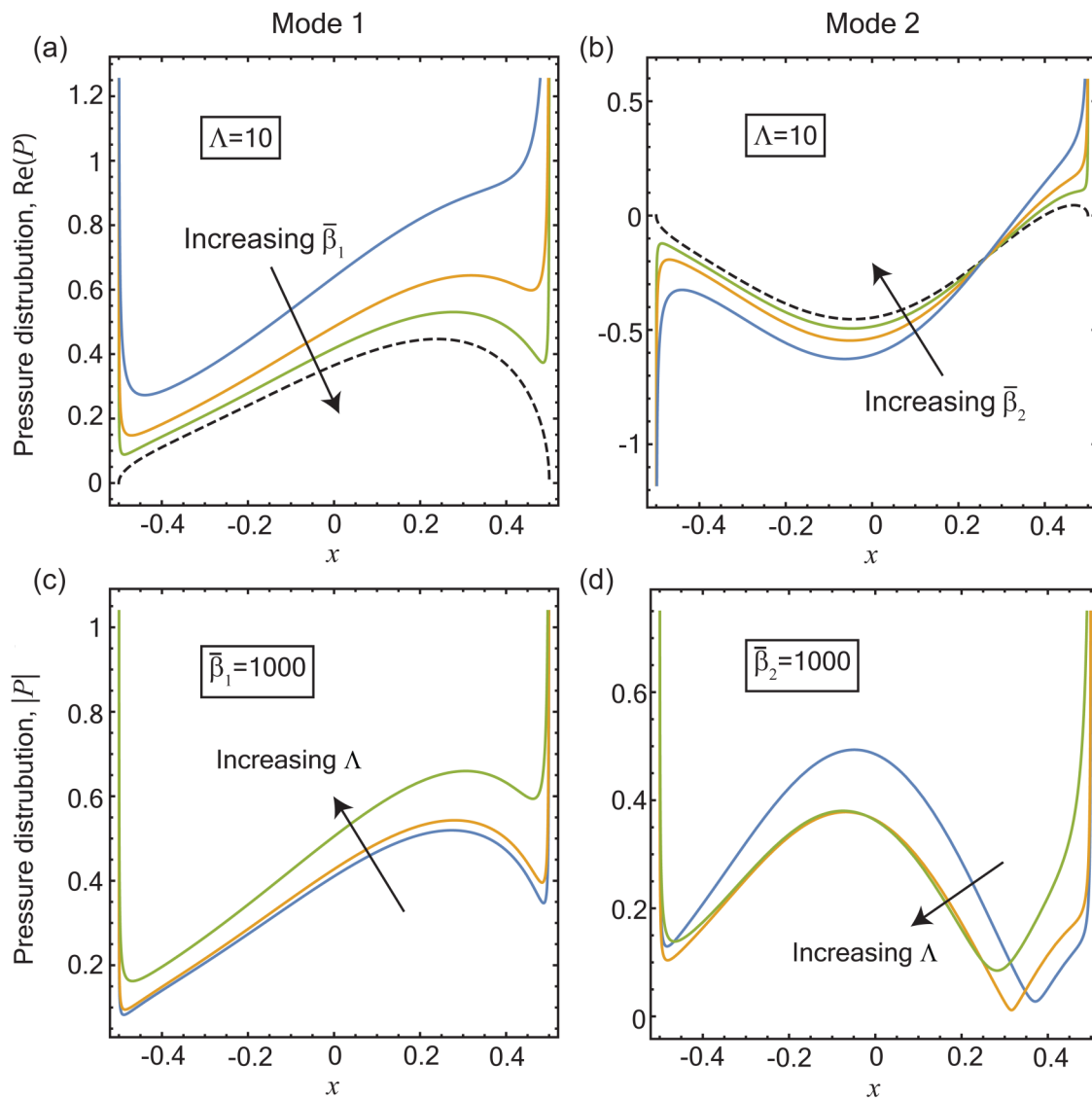
B. Normalized deflection functions

Figure 4 illustrates the effect of hydrodynamic loading on the deflection function (mode shape), $w(x)$, of a cantilevered sheet of zero aspect ratio, for modes $n=1, 2$ and 3 . Results are given as a function of the added mass parameter, Λ , and normalized Reynolds number, $\bar{\beta}_n$. These data show that the deflection function of the fundamental mode ($n=1$), normalized by $|w(1/2)|$, is relatively insensitive to fluid loading in comparison to the higher order modes,

$n=2$ and 3 . Increasing the effects of viscosity (i.e., decreasing $\bar{\beta}_n$) or the strength of fluid loading (i.e., increasing Λ) is observed to enhance the effect of the fluid surrounding the cantilevered plate.

C. Viscous theory of Atkinson and Manrique de Lara²⁸

Atkinson and Manrique de Lara²⁸ developed a theory for the fluid-structure interaction of a zero-aspect-ratio cantilevered plate immersed in an inviscid fluid and proposed a correction to account for the effect of small viscosity, i.e., $\beta \gg 1$. Specifically, they assumed that the hydrodynamic pressure load, $P(x)$, experienced by the cantilevered plate could be expanded in powers of $1/\sqrt{\beta}$, which was solved using the Wiener-Hopf method. For the present problem, this approach gives [see Sec. SM 3 of the [supplementary material](#) for its derivation]



09 October 2023 17:49:51

FIG. 3. Dimensionless pressure distribution, $P(x)$ —according to Eqs. (4) and (23)—experienced by the cantilevered plate for the first two modes, $n = 1, 2$. The mode shapes, $w(x)$, are scaled such that $|w(1/2)| = 1$. (a) and (b) Real part of the pressure for increasing normalized Reynolds number $\bar{\beta}_n = 25, 158$, and 1000 , at a constant added mass parameter, $\Lambda = 10$. Dashed lines are the inviscid solution ($\beta \rightarrow \infty$). (c) and (d) Magnitude of $P(x)$ at constant $\bar{\beta}_n = 1000$, for increasing $\Lambda = 0.01, 1$, and 100 , corresponding to light, medium, and heavy fluid load conditions, respectively.

$$P(x) = P_{inv}(x) + \sqrt{\frac{2}{\beta}}(1+i) \left(\frac{D_0}{\sqrt{1+2x}} + \frac{D_1}{\sqrt{1-2x}} \right), \quad (36)$$

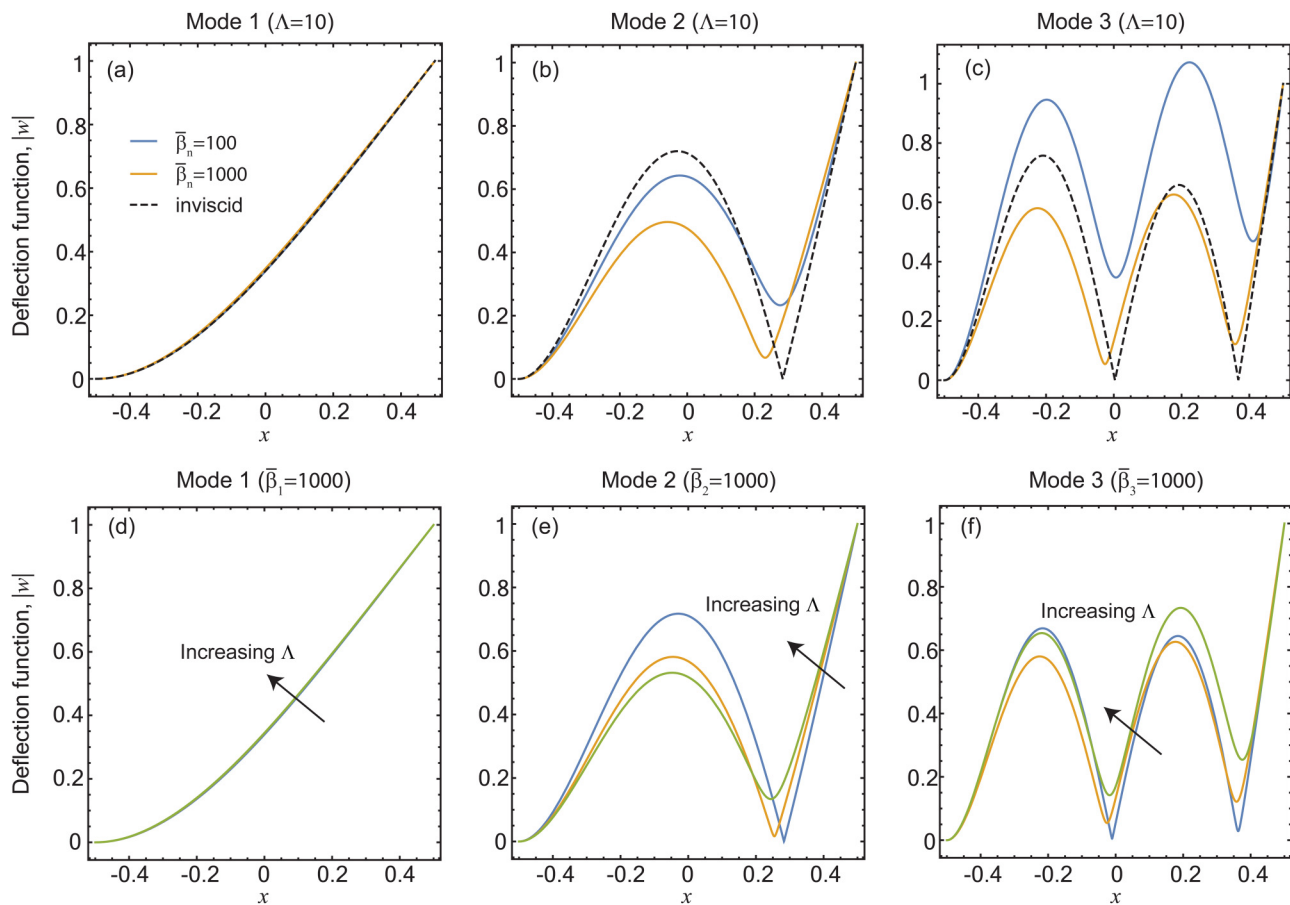
where²⁹

$$P_{inv}(x) = -\frac{2}{\pi} \int_{-\frac{1}{2}}^{\frac{1}{2}} w(\xi) \log \left| \frac{\sqrt{(1-2x)(1+2\xi)} - \sqrt{(1-2\xi)(1+2x)}}{\sqrt{(1-2x)(1+2\xi)} + \sqrt{(1-2\xi)(1+2x)}} \right| d\xi \quad (37)$$

and

$$D_0 = \frac{2}{\pi} \int_{-\frac{1}{2}}^{\frac{1}{2}} w(\xi) \sqrt{\frac{1-2\xi}{1+2\xi}} d\xi, \quad D_1 = \frac{2}{\pi} \int_{-\frac{1}{2}}^{\frac{1}{2}} w(\xi) \sqrt{\frac{1+2\xi}{1-2\xi}} d\xi. \quad (38)$$

The resonant frequencies and quality factors of the cantilevered plate follow analogously from the analysis in Sec. II C.



09 October 2023 17:49:51

FIG. 4. Mode shapes of a cantilevered plate of zero aspect ratio, for $n = 1, 2$, and 3 , showing the effect of fluid immersion. Magnitude of deflection functions, $|w|$, for (a)–(c) normalized Reynolds numbers, $\bar{\beta}_n = 100, 1000$, and ∞ (inviscid flow) at fixed added mass parameter $\Lambda = 10$, and (d)–(f) increasing added mass parameter, $\Lambda = 0, 1$, and 100 at fixed $\bar{\beta}_n = 1000$. Mode shapes are normalized to unity at the free end of the cantilevered plate, $x = 1/2$.

D. Comparison to finite-element-method simulations

The finite element (FE) method is implemented using the eigenfrequency solver of the commercial software, COMSOL Multiphysics, to generate independent and high accuracy numerical solutions. Deformation of the cantilevered plate is modeled using Navier's equation for an elastic solid, while motion of the surrounding fluid is specified by Eq. (8). The usual conditions of stress and velocity continuity are imposed at the interface between the fluid and solid domains. The plate thickness is systematically reduced to recover the thin plate assumption of the theoretical model in Sec. II; a thickness-to-length ratio of 0.01 is used for the results that follow. The FE mesh and fluid domain boundary are systematically refined to achieve the unbounded flow domain assumption, while reaching a convergence of at least 99.9% in the resonant frequencies and 99% in the quality factors.

Figure 5 shows a comparison of the complementary theories of Sec. II and Atkinson and Manrique de Lara²⁸ to independent

numerical results of the two-dimensional FE method; data are shown for the fundamental mode, $n = 1$. Results are given as a function of the normalized Reynolds number, $\bar{\beta}_1$, for an added mass parameter of $\Lambda = 0.001$ and 1 , corresponding to light fluid loading (e.g., for a gas) and heavy fluid loading (e.g., for a liquid), respectively. In all cases, the present theory in Sec. II precisely matches the independent results of the FE method, whereas the theory of Atkinson and Manrique de Lara²⁸ significantly underestimates the FE results. This difference is likely due to invalidity of the thin boundary layer assumption used in Ref. 28 near the plate edges at $|x| = 1/2$, where a local Stokes flow can induce non-algebraic corrections to the large- β asymptotic solution of Sec. III C. This is consistent with the observation that the Atkinson and Manrique de Lara theory does approach the present theory and FE method results as $\bar{\beta}_1$ increases, albeit slowly. Computational limitations restrict our ability to make a comparison at larger values of $\bar{\beta}_1$.

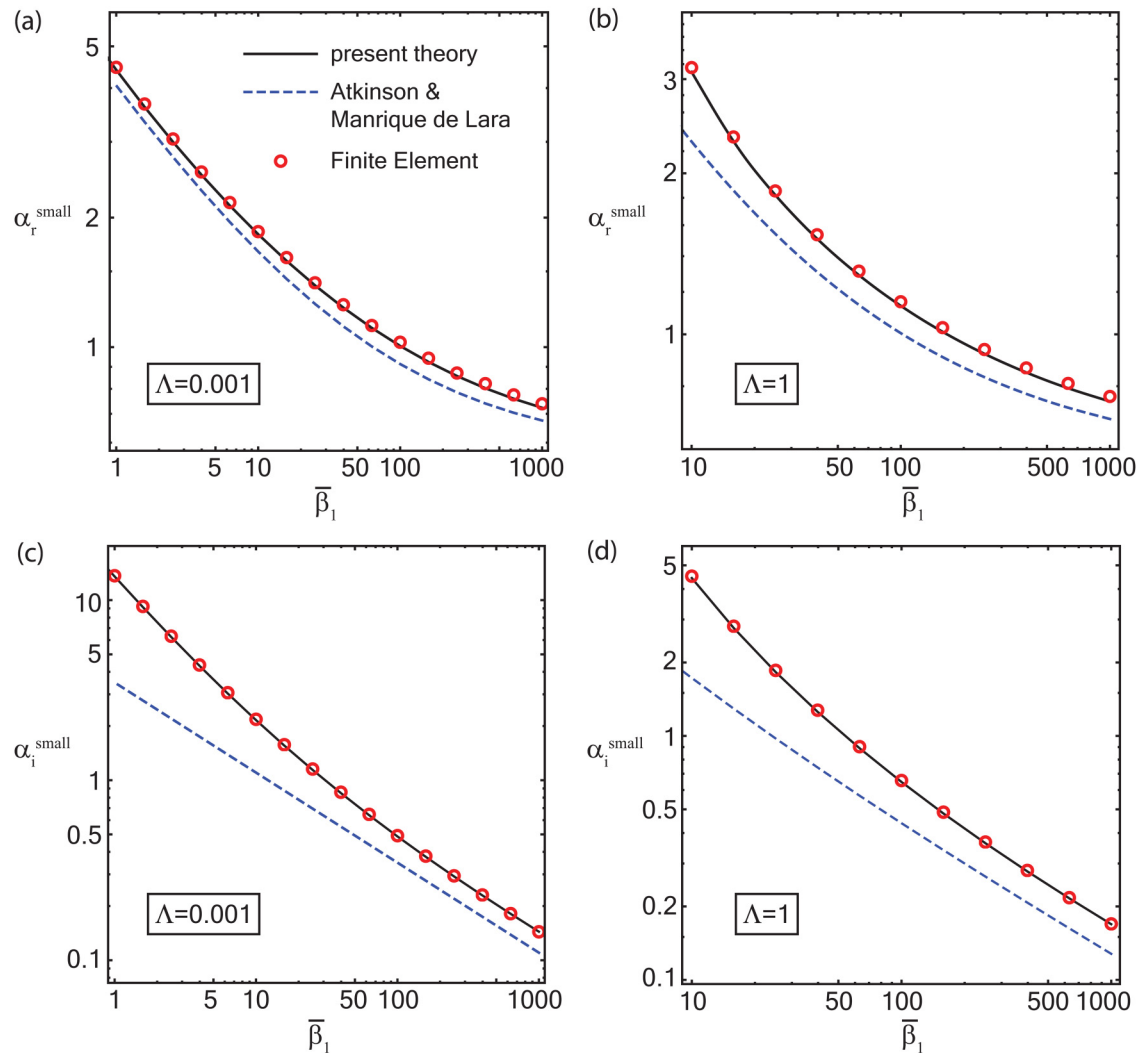


FIG. 5. Real and imaginary parts of the rescaled hydrodynamic function, α_{small} —denoted by subscripts r and i —for the fundamental mode ($n = 1$), as a function of the normalized Reynolds number, $\bar{\beta}_1$. Present theory of Sec. II (solid lines); theory of Atkinson and Manrique de Lara²⁸ (dashed lines); and independent two-dimensional FE method simulations (open circles). (a) and (c) Light fluid loading, $\Lambda = 0.001$ (e.g., for a gas); (b) and (d) heavy fluid loading, $\Lambda = 1$ (e.g., for a liquid).

IV. NUMERICAL RESULTS FOR ARBITRARY ASPECT RATIO

In this section, the FE method simulations are extended to the three-dimensional case of a cantilevered plate of finite aspect ratio, L/b , oscillating in its flexural modes. Again, a thickness-to-length ratio of $h/L = 0.01$ is used throughout, and the FE mesh and flow domain are systematically refined to achieve identical convergence to that of two-dimensional simulations. Numerical results are computed for aspect ratios ranging from $L/b = 0.1$ –20 by fixing the cantilever length and reducing its width. This leads to a systematic degradation of the thin plate assumption as the aspect ratio increases, with a thickness-to-width ratio of $h/b = 0.2$ for the

largest aspect ratio. These numerical results are used to benchmark the range of validity of the small (zero) aspect ratio theory in Sec. II. Comparison is also made with the large (infinite) aspect ratio theory of Sader,¹⁸ where the hydrodynamic function for finite thickness-to-width ratio reported in Table 1 of Brumley *et al.*³⁰ is used in Eq. (32).

Figure 6 gives corresponding results for the resonant frequency, $\omega_{R,n}$, and quality factor, Q_n , of the first two modes, $n = 1$ and 2, as a function of the plate aspect ratio, L/b . The added mass parameter used in Fig. 6 is varied to span the values typically encountered in practice,^{5,18} i.e., $\Lambda = 0.01$, 0.1, and 1, representing light, medium, and heavy fluid loading. Results are presented for fixed $\bar{\beta}_n$, which aligns with the fixed cantilever length, L , used in

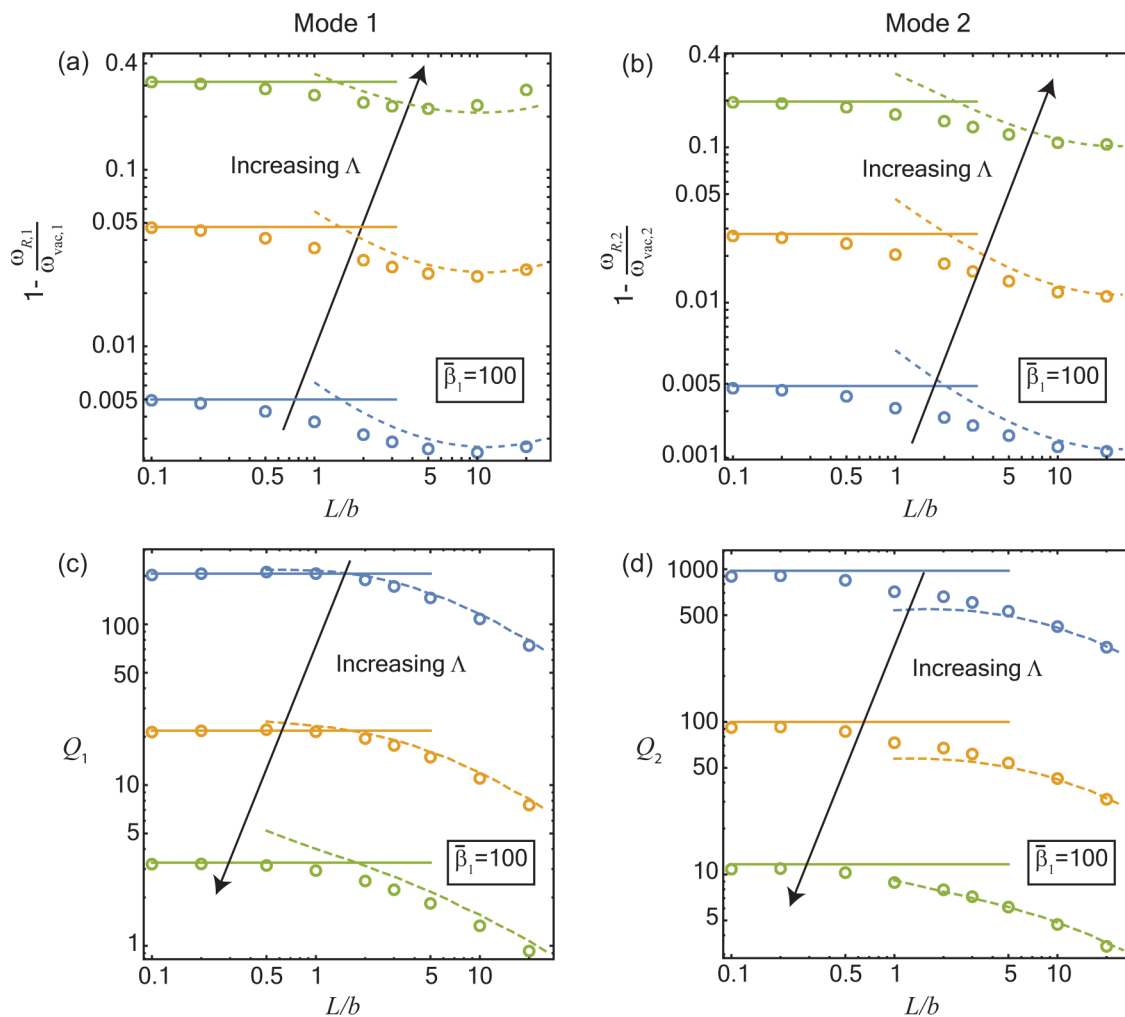


FIG. 6. (a) and (b) Change in resonant frequency, $\omega_{R,n}$, relative to the frequency in vacuum, $\omega_{vac,n}$; and (c) and (d) quality factor, Q_n ; for the first two modes, $n = 1$ and 2, as a function of aspect ratio, L/b . The rescaled Reynolds number is fixed at $\bar{\beta}_1 = 100$, while the added mass parameter is varied, $\Lambda = 0.01, 0.1$, and 1. FE method results (open circles); zero-aspect-ratio theory of Sec. II (solid lines); and large (infinite) aspect ratio theory of Refs. 18 and 30 (dashed lines).

simulations, mimicking experiments conducted under a similar scenario where the plate thickness, length, material, and fluid properties are fixed and the plate width is varied.

The asymptotic theories for small and large aspect ratios, mentioned above, accurately predict the FE numerical results in their respective regimes and to an aspect ratio of approximately one. The discrepancy between the large aspect ratio asymptotic theory and the FE method in Fig. 6(a) is due to the quality factor being approximately one [Fig. 6(c)], which is the threshold of validity for the eigenfrequency analysis; see discussion following Eq. (31) and Sec. III A.³⁴ The decrease in quality factor with increasing aspect ratio, L/b , observed in Figs. 6(c) and 6(d), is due to the width, b , being reduced at fixed length, L , in FE method simulations.

Figure 7 gives results analogous to Fig. 6, but where the cantilever length is first reduced, then its width varied to adjust the aspect ratio (still at a fixed thickness-to-length ratio of 0.01), which increases $\bar{\beta}_n$; results are given only for $\Lambda = 0.1$ and $n = 1$ for simplicity. Again, a good agreement is observed between the zero-aspect-ratio theory of Sec. II and FE method results, even up to an aspect ratio of approximately one; similar agreement is observed for the large aspect ratio theory of Refs. 18 and 30. Together with Fig. 6, these results demonstrate that the zero-aspect-ratio theory reported in this study accurately captures the true dynamics of a cantilevered plate of small aspect ratio, as its size and dimensions are varied. It is also generally observed that reducing the aspect ratio L/b enhances the Q -factors up to a limiting value, confirming recent numerical findings of Gesing *et al.*²⁶

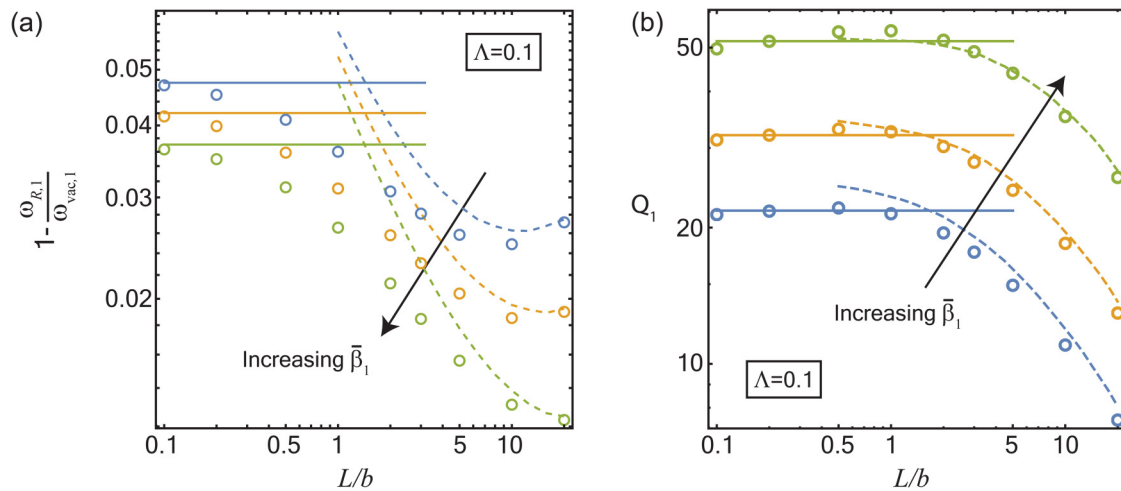


FIG. 7. (a) and (b) Change in resonant frequency, $\omega_{R,1}$, relative to the frequency in vacuum, $\omega_{vac,1}$; and (c) and (d) quality factor, Q_1 ; for the first mode, $n = 1$, as a function of aspect ratio, L/b . The added mass parameter is fixed at $\Lambda = 0.1$ and results are given for $\beta_1 = 100, 200$, and 500 . FE method results (open circles); zero-aspect-ratio theory of Sec. II (solid lines); and large (infinite) aspect ratio theory of Refs. 18 and 30 (dashed lines).

V. CONCLUSIONS

An exact analytical theory has been developed for the dynamic response of a cantilevered plate of zero aspect ratio that is immersed in a viscous fluid. The cantilevered plate was line clamped, and its resonant flexural oscillations were considered. The present theory was compared to that of Atkinson and Manrique de Lara,²⁸ developed in the small viscosity limit, where significant differences were observed. The relative accuracy of these complementary theories was clarified using high accuracy two-dimensional FE method simulations of this fluid-structure interaction, which were found to coincide with the present theory. The origin of the discrepancy between these theories is likely due to the thin viscous-penetration-depth assumption used in Ref. 28, which cannot hold near the (sharp) edges of the plate.

FE method simulations were also performed for cantilevered plates of finite aspect ratio. These three-dimensional simulations were used to assess the range of validity of the present theory, as a function of aspect ratio. It was observed that the present theory for zero aspect ratio exhibits good accuracy as the aspect ratio is varied, up to a value of approximately one. Similar behavior was found for the existing large aspect ratio theory,^{18,30} as has been reported previously.¹⁹ This shows that the dynamic response of cantilevers of finite aspect ratio can be well estimated by combining theories for zero and large aspect ratio. The findings of this study are expected to be of practical value in cantilever sensor design and application.

SUPPLEMENTARY MATERIAL

See the [supplementary material](#) for additional numerical results and derivation of Eq. (36).

ACKNOWLEDGMENTS

The authors gratefully acknowledge support of the Australian Research Council Grants Scheme.

AUTHOR DECLARATIONS

Conflict of Interest

The authors have no conflicts to disclose.

Author Contributions

Naijian Shen: Data curation (equal); Formal analysis (equal); Investigation (equal); Methodology (equal); Writing – original draft (equal); Writing – review & editing (equal). **Debadri Chakraborty:** Formal analysis (equal); Investigation (equal); Validation (equal); Writing – review & editing (equal). **John E. Sader:** Conceptualization (equal); Formal analysis (equal); Investigation (equal); Supervision (equal); Writing – review & editing (equal).

DATA AVAILABILITY

The data that support the findings of this study are available from the corresponding author upon reasonable request.

APPENDIX A: ALTERNATE SOLUTION FOR THE INVISCID FLOW

In this Appendix, we report an alternate solution to that of Ref. 29 for the resonant frequencies of a zero-aspect-ratio cantilevered plate immersed in an inviscid fluid. This solution is based on the approach used for the viscous solution in Secs. II B 1 and II B 2, employing a slight modification to the ansatz in Eq. (22).

In the inviscid limit, $\beta \rightarrow \infty$, Eq. (15) gives the two-dimensional potential flow field and pressure distribution generated by the cantilevered plate,

$$u_z = -i \int_0^\infty \lambda [\chi(\lambda) \cos(\lambda x) + \psi(\lambda) \sin(\lambda x)] e^{-\lambda z} d\lambda, \quad (\text{A1a})$$

$$p = - \int_0^\infty [\chi(\lambda) \cos(\lambda x) + \psi(\lambda) \sin(\lambda x)] e^{-z\lambda} d\lambda, \quad (\text{A1b})$$

where χ and ψ are again to be determined from the boundary conditions in Eq. (16). In analogy with Eqs. (18) and (19), a pair of kernels, $\chi_k(\lambda)$ and $\psi_k(\lambda)$, are defined such that

$$\int_0^\infty \lambda \chi_k \cos(\lambda x) d\lambda = \Phi_k^{\text{even}}(x), \quad \int_0^\infty \lambda \psi_k \sin(\lambda x) d\lambda = \Phi_k^{\text{odd}}(x), \quad (\text{A2})$$

for $|x| \leq 1/2$, and

$$\int_0^\infty \lambda \chi_k \cos(\lambda x) d\lambda = \int_0^\infty \lambda \psi_k \sin(\lambda x) d\lambda = 0, \quad |x| > \frac{1}{2}, \quad (\text{A3})$$

with the complete kernels following from Eq. (21).

Unlike the viscous solution, the pressure distribution vanishes at the edges of the plate. This necessitates use of a different ansatz for $\chi_k(\lambda)$ and $\psi_k(\lambda)$ to satisfy Eq. (A3),^{15,17} namely,

$$\chi_k(\lambda) = \sum_{m=1}^M b_{m,k} \frac{J_{2m-1}(\frac{\lambda}{2})}{\lambda}, \quad \psi_k(\lambda) = \sum_{m=1}^M c_{m,k} \frac{J_{2m}(\frac{\lambda}{2})}{\lambda}. \quad (\text{A4})$$

The pressure distribution along the upper surface of the plate is determined using Eq. (A1b), giving

$$p(x, 0^+) = - \sum_{n=1}^N a_n H_n(x), \quad (\text{A5})$$

where

$$H_k(x) = \sum_{m=1}^M \left[b_{m,k} \frac{T_{2m-1}(\sqrt{1-4x^2})}{2m-1} + c_{m,k} \frac{x U_{2m-1}(\sqrt{1-4x^2})}{m} \right]. \quad (\text{A6})$$

To determine the coefficients $b_{m,k}$ and $c_{m,k}$, Eqs. (A2) and (A4) produce

$$\sum_{m=1}^M b_{m,k} \frac{2T_{2m-1}(\sqrt{1-4x^2})}{\sqrt{1-4x^2}} = \Phi_k^{\text{even}}(x), \quad (\text{A7})$$

$$\sum_{m=1}^M c_{m,k} \frac{4x U_{2m-1}(\sqrt{1-4x^2})}{\sqrt{1-4x^2}} = \Phi_k^{\text{odd}}(x),$$

where $b_{m,k}$ and $c_{m,k}$ are specified by the orthogonal property of Chebyshev polynomials, giving

$$b_{m,k} = \frac{2}{\pi} \int_{-\frac{1}{2}}^{\frac{1}{2}} \Phi_k^{\text{even}}(x) T_{2m-1}(\sqrt{1-4x^2}) dx, \quad (\text{A8a})$$

$$c_{m,k} = \frac{4}{\pi} \int_{-\frac{1}{2}}^{\frac{1}{2}} x \Phi_k^{\text{odd}}(x) U_{2m-1}(\sqrt{1-4x^2}) dx. \quad (\text{A8b})$$

The resonant frequencies are solved by substituting pressure distribution, Eq. (A5), into the plate deflection equation, Eq. (1), giving the required eigenvalue equation,

$$\sum_{k=1}^N a_k \left[\left(\frac{C_k^4}{C_n^4} - \Omega_n^2 \right) \delta_{jk} - 2\Omega_n^2 \Lambda \int_{-\frac{1}{2}}^{\frac{1}{2}} \Phi_j H_k dx \right] = 0, \quad (\text{A9})$$

where $n, j = 1, 2, \dots, N$.

APPENDIX B: IMPROPER INTEGRALS EXPRESSED AS MEIJER G-FUNCTIONS

Meijer G -functions were used in Ref. 22 to specify the flow generated by an oscillating plate. The derivation of such functions is clarified in this Appendix.

Equation (26) originates from two improper integrals,

$$B_{q,m} = \lim_{\kappa \rightarrow 0} \int_0^\infty \lambda^{2q-2} \sqrt{\lambda^2 + \kappa^2} \left(1 - \frac{\sqrt{\lambda^2 + \kappa^2}}{\sqrt{\lambda^2 + \kappa^2 - i\beta}} \right) J_{2m-2} \left(\frac{\lambda}{2} \right) d\lambda, \quad (\text{B1a})$$

$$C_{q,m} = \lim_{\kappa \rightarrow 0} \int_0^\infty \lambda^{2q-1} \sqrt{\lambda^2 + \kappa^2} \left(1 - \frac{\sqrt{\lambda^2 + \kappa^2}}{\sqrt{\lambda^2 + \kappa^2 - i\beta}} \right) J_{2m-1} \left(\frac{\lambda}{2} \right) d\lambda. \quad (\text{B1b})$$

The modern definition of the G -function is given in Ref. 35 in terms of a complex contour integral. This is an extension upon general hypergeometric functions to include most of the known functions as special cases.^{36–38} In particular, the following identities from Ref. 37 are needed to evaluate Eq. (B1),

$$(1+x)^\alpha = \frac{1}{\Gamma(-\alpha)} G_{1,1}^{1,1} \left(x \middle| \begin{matrix} \alpha+1 \\ 0 \end{matrix} \right), \quad (\text{B2a})$$

$$x^\mu J_\nu(x) = 2^\mu G_{0,2}^{1,0} \left(\frac{x^2}{4} \middle| \begin{matrix} \frac{1}{2}(\mu+\nu), \frac{1}{2}(\mu-\nu) \end{matrix} \right), \quad (\text{B2b})$$

where Γ is the Gamma function here (not the hydrodynamic function) and J_ν is the Bessel function of the first kind of order ν . A remarkable property, that makes G -functions important in algorithmic definite integral evaluation, is that the family of G -functions is closed under a wide range of operations.³⁵ Here, we use the absorption closure under a multiplication by power-laws,

$$x^\mu G_{p,q}^{m,n} \left(x \middle| \begin{matrix} \mathbf{a}_p \\ \mathbf{b}_q \end{matrix} \right) = G_{p,q}^{m,n} \left(x \middle| \begin{matrix} \mathbf{a}_p + \mu \mathbf{1}_p \\ \mathbf{b}_q + \mu \mathbf{1}_q \end{matrix} \right), \quad (\text{B3})$$

where \mathbf{a}_p and \mathbf{b}_q are sequences of numbers of length p and q , respectively, while $\mathbf{1}_p$ is a sequence of ones of length p . We also use

the following closure under integral convolution:

$$\begin{aligned} & \int_0^\infty G_{p,q}^{m,n} \left(\eta x \left| \begin{matrix} \mathbf{a}_p \\ \mathbf{b}_q \end{matrix} \right. \right) G_{\sigma,\tau}^{\mu,\nu} \left(\omega x \left| \begin{matrix} \mathbf{c}_\sigma \\ \mathbf{d}_\tau \end{matrix} \right. \right) dx \\ &= \frac{1}{\eta} G_{q+\sigma, p+\tau}^{n+\mu, m+\nu} \left(\frac{\omega}{\eta} \left| \begin{matrix} -b_1, \dots, -b_m, \mathbf{c}_\sigma, -b_{m+1}, \dots, -b_q \\ -a_1, \dots, -a_n, \mathbf{d}_\tau, -a_{n+1}, \dots, -a_p \end{matrix} \right. \right) \\ &= \frac{1}{\omega} G_{p+\tau, q+\sigma}^{m+\nu, n+\mu} \left(\frac{\eta}{\omega} \left| \begin{matrix} a_1, \dots, a_n, -\mathbf{d}_\tau, a_{n+1}, \dots, a_p \\ b_1, \dots, b_m, -\mathbf{c}_\sigma, b_{m+1}, \dots, b_q \end{matrix} \right. \right). \end{aligned} \quad (\text{B4})$$

The convergence of such integrals is discussed in Refs. 35 and 36. These closures facilitate the analytic evaluation of the improper integrals in Eq. (B1), as follows.

For $B_{q,m}$, the integral of interest can be decomposed as

$$B_{q,m} = \lim_{\kappa \rightarrow 0} (i_1 + i_2 + i_3), \quad (\text{B5})$$

where

$$i_1 = \int_0^\infty \lambda^{2q-2} \sqrt{\kappa^2 + \lambda^2} J_{2m-2} \left(\frac{\lambda}{2} \right) d\lambda, \quad (\text{B6a})$$

$$i_2 = -\kappa^2 \int_0^\infty \frac{\lambda^{2q-2}}{\sqrt{\kappa^2 + \lambda^2 - i\beta}} J_{2m-2} \left(\frac{\lambda}{2} \right) d\lambda, \quad (\text{B6b})$$

$$i_3 = -\int_0^\infty \frac{\lambda^{2q}}{\sqrt{\kappa^2 + \lambda^2 - i\beta}} J_{2m-2} \left(\frac{\lambda}{2} \right) d\lambda. \quad (\text{B6c})$$

Using Eq. (B2), each of the integrands in $i_{1,2,3}$ is expressible as the product of two G -functions; hence, the convolution formula, Eq. (B4), and the absorption formula, Eq. (B3), give the required results,

$$i_1 = -\frac{4^{2q-1}}{\sqrt{\pi}} G_{1,3}^{2,1} \left(\frac{\kappa^2}{16} \left| \begin{matrix} \frac{3}{2} \\ 0, q+m-1, q-m+1 \end{matrix} \right. \right), \quad (\text{B7a})$$

$$i_2 = -\frac{2^{4q-5} \kappa^2}{\sqrt{\pi}} G_{1,3}^{2,1} \left(\frac{\kappa^2 - i\beta}{16} \left| \begin{matrix} \frac{1}{2} \\ 0, q+m-2, q-m \end{matrix} \right. \right), \quad (\text{B7b})$$

$$i_3 = -\frac{2^{4q-1}}{\sqrt{\pi}} G_{1,3}^{2,1} \left(\frac{\kappa^2 - i\beta}{16} \left| \begin{matrix} \frac{1}{2} \\ 0, q+m-1, q-m+1 \end{matrix} \right. \right). \quad (\text{B7c})$$

Equation (26b) follows directly under transforms, $m \mapsto m + \frac{1}{2}$ and $q \mapsto q + \frac{1}{2}$.

APPENDIX C: SMALL STRENGTH OF THE FLUID LOADING LIMIT

In this Appendix, we derive an asymptotic formula for the rescaled hydrodynamic function, α_{small} , of the fundamental mode ($n = 1$), in the small strength of the fluid loading limit, i.e., $\Lambda \ll 1$.

TABLE II. Comparison of α^{small} obtained using (i) the $\Lambda \rightarrow 0$ asymptotic formula in Eq. (C3) and (ii) the full numerical solution in Eq. (29) for $\Lambda = 0.001$.

$\log_{10} \bar{\beta}_1$	Eq. (C3)	Eq. (29) for $\Lambda = 0.001$
3	0.722 905 + 0.144037 <i>i</i>	0.722 949 + 0.144042 <i>i</i>
2.5	0.828 325 + 0.258471 <i>i</i>	0.828 391 + 0.258542 <i>i</i>
2	1.006 22 + 0.486929 <i>i</i>	1.006 37 + 0.487117 <i>i</i>
1.5	1.308 74 + 0.981469 <i>i</i>	1.309 13 + 0.982045 <i>i</i>
1	1.827 93 + 2.15386 <i>i</i>	1.829 09 + 2.15591 <i>i</i>
0.5	2.737 67 + 5.17863 <i>i</i>	2.741 61 + 5.18700 <i>i</i>
0	4.393 28 + 13.5036 <i>i</i>	4.408 51 + 13.5424 <i>i</i>
−0.5	7.578 75 + 37.4374 <i>i</i>	7.644 06 + 37.6400 <i>i</i>
−1	14.1305 + 108.157 <i>i</i>	14.4300 + 109.343 <i>i</i>
−1.5	28.4963 + 320.766 <i>i</i>	29.9801 + 328.623 <i>i</i>
−2	61.6960 + 967.349 <i>i</i>	74.8036 + 1034.19 <i>i</i>

To leading order in small Λ , the mode shape of the cantilevered plate in fluid, $w(x)$, can be replaced by the mode shape in vacuum, i.e., $w(x) \mapsto \Phi(x)$, i.e., $a_k = 0$ for all $k \geq 2$ in Eqs. (17) and (23), with Eq. (29) becoming

$$\Omega_1^2 = \left(1 + 2\Lambda \int_{-\frac{1}{2}}^{\frac{1}{2}} \Phi_1(x) H_1(x|\beta) dx \right)^{-1}, \quad (\text{C1})$$

where $\beta = \Omega_1 \bar{\beta}_1$. Expanding Eq. (C1) in the small parameter, Λ , gives

$$\Omega_1 = 1 - \Lambda \int_{-\frac{1}{2}}^{\frac{1}{2}} \Phi_1(x) H_1(x|\beta = \bar{\beta}_1) dx + o(\Lambda), \quad (\text{C2})$$

where the series representation of $H_1(x)$ in Eq. (24) can now be evaluated explicitly using Eq. (25) for a given $\beta = \bar{\beta}_1$. Hence, it follows from Eq. (34) that

$$\alpha^{\text{small}} = 2 \int_{-\frac{1}{2}}^{\frac{1}{2}} \Phi_1(x) H_1(x|\beta = \bar{\beta}_1) dx + o(1), \quad (\text{C3})$$

which is independent of Λ . This theoretical prediction is borne out in the full numerical solution plotted in Fig. 2, where α_{small} asymptotes to a constant value as $\Lambda \rightarrow 0$ for fixed $\bar{\beta}_1$.

Equation (C3) is compared with the full numerical solution, Eq. (29), in Table II for small and fixed Λ . While $\Omega_1 \rightarrow 1$ as $\Lambda \rightarrow 0$, i.e., in vacuum, its asymptotic rate of convergence decreases as $\bar{\beta}_1$ is reduced to small values, at fixed nonzero Λ ; with $\Omega_1 \rightarrow 0$ as $\bar{\beta}_1 \rightarrow 0$ for any small but finite Λ , as per Eq. (C1). This property is borne out in Table II where excellent agreement is observed, except for the smallest values of $\bar{\beta}_1$.

REFERENCES

- G. Binnig, C. F. Quate, and C. Gerber, "Atomic force microscope," *Phys. Rev. Lett.* **56**, 930 (1986).

- ²J. E. Sader, J. W. M. Chon, and P. Mulvaney, "Calibration of rectangular atomic force microscope cantilevers," *Rev. Sci. Instrum.* **70**, 3967 (1999).
- ³C. P. Green and J. E. Sader, "Frequency response of cantilever beams immersed in viscous fluids near a solid surface with applications to the atomic force microscope," *J. Appl. Phys.* **98**, 114913 (2005).
- ⁴T. Fukuma, "Wideband low-noise optical beam deflection sensor with photo-thermal excitation for liquid-environment atomic force microscopy," *Rev. Sci. Instrum.* **80**, 023707 (2009).
- ⁵C. A. Van Eysden and J. E. Sader, "Frequency response of cantilever beams immersed in viscous fluids with applications to the atomic force microscope: Arbitrary mode order," *J. Appl. Phys.* **101**, 044908 (2007).
- ⁶F. Cellini, C. Intartaglia, L. Soria, and M. Porfiri, "Effect of hydrodynamic interaction on energy harvesting in arrays of ionic polymer metal composites vibrating in a viscous fluid," *Smart Mater. Struct.* **23**, 045015 (2014).
- ⁷J. E. Sader, T. P. Burg, and S. R. Manalis, "Energy dissipation in microfluidic beam resonators," *J. Fluid Mech.* **650**, 215–250 (2000).
- ⁸G. Katsikis, J. F. Collis, S. M. Knudsen, V. Agache, J. E. Sader, and S. R. Manalis, "Inertial and viscous flywheel sensing of nanoparticles," *Nat. Commun.* **12**, 1–6 (2021).
- ⁹H. G. Craighead, "Nanoelectromechanical systems," *Science* **290**, 1532 (2000).
- ¹⁰J. L. Arlett, E. B. Myers, and M. L. Roukes, "Comparative advantages of mechanical biosensors," *Nat. Nanotechnol.* **6**, 203 (2011).
- ¹¹M. S. Hanay, S. I. Kelber, C. D. O'Connell, P. Mulvaney, J. E. Sader, and M. L. Roukes, "Inertial imaging with nanomechanical systems," *Nat. Nanotechnol.* **10**, 339–344 (2015).
- ¹²W. H. Chu, Tech. Rep. No. 2, DTMB, Contract NObs-86396(X) (Southwest Research Institute, San Antonio, Texas, 1963).
- ¹³U. S. Lindholm, D. D. Kana, W. H. Chu, and H. Abramson, "Elastic vibration characteristics of cantilever plates in water," *J. Ship Res.* **9**, 11–22 (1965).
- ¹⁴D. G. Crighton, "Resonant oscillations of fluid-loaded struts," *J. Sound Vib.* **87**, 429–437 (1983).
- ¹⁵C. A. Van Eysden and J. E. Sader, "Resonant frequencies of a rectangular cantilever beam immersed in a fluid," *J. Appl. Phys.* **100**, 114916 (2006).
- ¹⁶E. O. Tuck, "Calculation of unsteady flows due to small motions of cylinders in a viscous fluid," *J. Eng. Math.* **3**, 29–44 (1969).
- ¹⁷F. J. Elmer and M. Dreier, "Eigenfrequencies of a rectangular atomic force microscope cantilever in a medium," *J. Appl. Phys.* **81**, 7709–7714 (1997).
- ¹⁸J. E. Sader, "Frequency response of cantilever beams immersed in viscous fluids with applications to the atomic force microscope," *J. Appl. Phys.* **84**, 64–76 (1998).
- ¹⁹J. W. Chon, P. Mulvaney, and J. E. Sader, "Experimental validation of theoretical models for the frequency response of atomic force microscope cantilever beams immersed in fluids," *J. Appl. Phys.* **87**, 3978–3988 (2000).
- ²⁰M. R. Paul and M. C. Cross, "Stochastic dynamics of nanoscale mechanical oscillators immersed in a viscous fluid," *Phys. Rev. Lett.* **92**, 235501 (2004).
- ²¹A. Maali, C. Hurth, T. Cohen-Bouhacina, G. Couturier, and J. P. Aimé, "Improved acoustic excitation of atomic force microscope cantilevers in liquids," *Appl. Phys. Lett.* **88**, 163504 (2006).
- ²²C. A. Van Eysden and J. E. Sader, "Small amplitude oscillations of a flexible thin blade in a viscous fluid: Exact analytical solution," *Phys. Fluids* **18**, 123102 (2006).
- ²³C. A. Van Eysden and J. E. Sader, "Compressible viscous flows generated by oscillating flexible cylinders," *Phys. Fluids* **21**, 013104 (2009).
- ²⁴C. A. Van Eysden and J. E. Sader, "Frequency response of cantilever beams immersed in compressible fluids with applications to the atomic force microscope," *J. Appl. Phys.* **106**, 094904 (2009).
- ²⁵G. Pfusterschmied, C. Weinmann, M. Schneider, D. Platz, N. Shen, J. Sader, and U. Schmid, "Sound dissipation from plate-type resonators excited in non-conventional transversal modes in liquids," *J. Micromech. Microeng.* **30**, 075004 (2020).
- ²⁶A. Gesing, D. Platz, and U. Schmid, "Viscous fluid–structure interaction of micro-resonators in the beam–plate transition," *J. Appl. Phys.* **131**, 134502 (2022).
- ²⁷W. Pabst, "Theory of the landing impact of seaplanes," N.A.C.A. Technical Memorandum 580 (1930).
- ²⁸C. Atkinson and M. M. de Lara, "The frequency response of a rectangular cantilever plate vibrating in a viscous fluid," *J. Sound Vib.* **300**, 352–367 (2007).
- ²⁹N. Shen, D. Chakraborty, and J. E. Sader, "Resonant frequencies of cantilevered sheets under various clamping configurations immersed in fluid," *J. Appl. Phys.* **120**, 144504 (2016).
- ³⁰D. R. Brumley, M. Willcox, and J. E. Sader, "Oscillation of cylinders of rectangular cross section immersed in fluid," *Phys. Fluids* **22**, 052001 (2010).
- ³¹S. P. Timoshenko and S. Woinowsky-Krieger, *Theory of Plates and Shells* (McGraw-Hill, 1959).
- ³²G. K. Batchelor, *An Introduction to Fluid Dynamics* (Cambridge University Press, 2000).
- ³³M. Abramowitz and I. A. Stegun, *Handbook of Mathematical Functions* (Dover, New York, 1972).
- ³⁴D. Chakraborty, E. van Leeuwen, M. Pelton, and J. E. Sader, "Vibration of nanoparticles in viscous fluids," *J. Phys. Chem. C* **117**, 8536–8544 (2013).
- ³⁵Y. L. Luke, *The Special Functions and Their Approximations* (Academic Press, New York, 1969), Vol. 1.
- ³⁶A. P. Prudnikov, Y. A. Brychkov, and O. I. Marichev, *Integrals and Series* (Gordon and Breach, Newark, NJ, 1986–1992), Vol. 5.
- ³⁷Bateman Manuscript Project, *Higher Transcendental Functions* (McGraw-Hill, New York, 1953–1955), Vol. 3.
- ³⁸A. M. Mathai and R. K. Saxena, *Generalized Hypergeometric Functions with Applications in Statistics and Physical Sciences* (Springer, Berlin, 1973).